Tensile Creep Behavior of SiC_f/SiC Ceramic Matrix Minicomposites

Amjad S. Almansour[1] and Gregory N. Morscher[2]

[1]NASA Glenn Research Center, Cleveland, Ohio

[2]The University of Akron, Akron, Ohio

*Corresponding author; E-mail address: amjad.s.almansour@nasa.gov; Tel.: +12164332971

Abstract

Single fiber-tow minicomposites represent the major load-bearing element of woven and laminate ceramic matrix composites (CMCs). To understand the effects of fiber type, fiber content, and matrix cracking on tensile creep in SiC_f/SiC CMCs, single-tow SiC_f/SiC minicomposites with different fiber types and contents were investigated. The minicomposites studied contained either Hi-Nicalon™ or Hi-Nicalon™ Type S SiC fibers with a boron nitride (BN) interphase and a chemical-vapor-infiltrated-silicon-carbide (CVI-SiC) matrix. Tensile creep was performed at 1200 °C in air. A bottom-up creep modeling approach was applied where creep parameters of the fibers and matrix were obtained separately at 1200 °C. Next, a theoretical model based on the rule of mixtures was derived to model the fiber and matrix creep-time-dependent stress redistribution. Fiber and matrix creep parameters, load transfer model results, and numerical modeling were used to construct a creep strain model to predict creep damage evolution of minicomposites with different fiber types and contents.

Keywords: SiC_f/SiC Minicomposites Creep, Creep Load Sharing Model, Total Creep Strain Model, Oxidation, Fiber Creep

1. Introduction

Silicon–carbide- (SiC-) based ceramic matrix composites (CMCs) offer an excellent combination of properties at high temperature such as high specific strength, chemical inertness, creep resistance, and irradiation tolerance. Those superior properties make SiC_f/SiC CMCs beneficial for use in high-temperature structural applications that are exposed to extreme environments such as hot-zone components of advanced turbine engines, leading-edge applications for hypersonic vehicles, and nuclear reactors [1–5].

The creep resistance of a SiC_f/SiC CMC depends on the individual constituent's creep resistance, creep resistance mismatch between CMC constituents, and the resulting time-temperature-load-dependent stress redistribution. It is also sensitive to microstructural features of the constituents (i.e., grain size, composition, pore size, and distribution) and depends greatly on applied stress, exposure time, temperature, and environment.

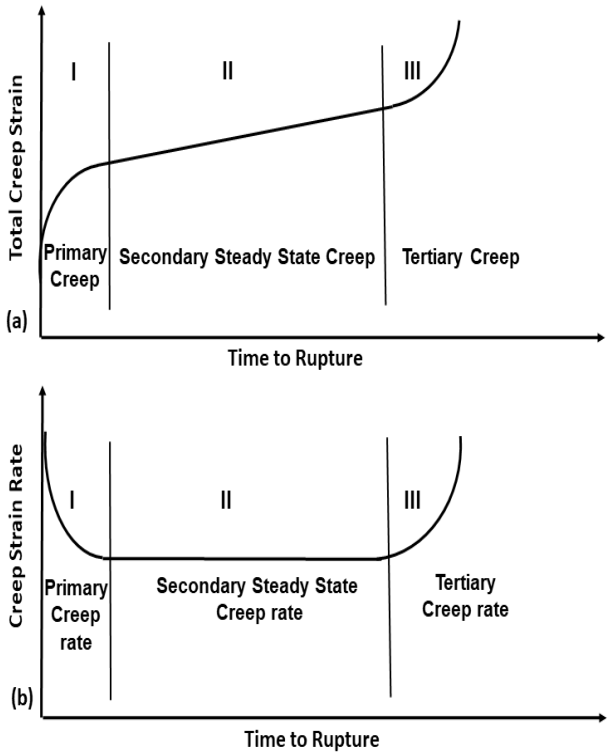

Fig. 1. Typical CMC behavior during a tensile creep test, showing (a) creep strain as a function of time to rupture and (b) creep strain rate as a function of time to rupture.

Typically, monolithic ceramics show three creep stages: primary (I), secondary (II), and tertiary (III) as shown in Fig. 1 [5]. They differ both macroscopically and microscopically in their behavior [6]. In the primary stage, the creep strain rate decreases with time until it plateaus at a constant value during the secondary stage. The decreasing creep strain rate is due to the buildup of internal elastic stresses as a result of grain-to-grain contact and alignment. During the primary stage, atomic diffusion occurs at the grain boundaries, which causes grain boundary sliding (Coble creep) [7,8]. This type of creep is time dependent and recoverable, and is characterized as viscoelastic deformation [8]. In the secondary stage, the buildup of internal elastic stresses can no longer be maintained due to presence of the internal diffusion phenomena. This leads to additional sliding at the grain boundary at a steady-state rate that is controlled by the diffusion (flow of vacancies) mechanism. Grain boundary diffusion can take place within the grain boundaries of the host material (Coble creep), and lattice diffusion takes place in the interior of the grains (Nabarro-Herring creep) [8]. The secondary stage is characterized as a time-dependent and nonrecoverable creep. Finally, in the tertiary creep stage, either cavity damage or internal voids at the grain boundary junctions

become large enough to contribute to a rapidly increased creep strain rate and to enhanced internal flaw growth resulting in rapid creep rupture of ceramics [6]. However, most ceramics don't experience the tertiary creep stage.

Second-generation SiC fibers such as Hi-Nicalon™ fiber and third-generation SiC fibers such as Hi-Nicalon™ Type S fiber are being used in high-temperature applications because of their low oxygen content, which enhances thermal and chemical stabilities at high temperatures. Additionally, their small diameter allows weaving and braiding multifilament tows into complex CMC fiber architectures without breaking the fibers [9]. Several studies characterized the composition and creep behavior of Hi-Nicalon™ and Hi-Nicalon™ Type S SiC fibers [9-17]. The Hi-Nicalon™ fiber consists of low-density nonstoichiometric 5-nm [10] β-SiC crystals, with 0.6 at.% excess oxygen, 57.8 at.% carbon, and 41.6 at.% silicon. [11]. However, the nonstoichiometric Hi-Nicalon™ fiber also contains a large excess of turbostratic carbon, which decreases the density [10] and affects its oxidation and creep behavior [11]. The Hi-Nicalon™ Type S fiber consists of high-density, polycrystalline, near-stoichiometric 100-nm [10] β-SiC crystals, with 0.2 at.% excess oxygen, 51 at.% carbon, and 48.7 at.% silicon [11] and less excess carbon than Hi-Nicalon™ fibers. Primary creep in Hi-Nicalon™ and Hi-Nicalon™ Type S fibers can be attributed to viscoelastic deformation of carbon at grain boundaries [12] that leads to SiC grain boundary sliding and dewrinkling as well as sliding of carbon crystallites [13]. Steady-state creep is attributed to the deformation of turbostratic carbon grain boundaries and diffusion of impurities at grain boundaries [12], which causes grain boundary sliding and ultimately diffusion of carbon or silicon within the grain [14]. Based on the compositions of Hi-Nicalon™ and Hi-Nicalon™ Type S fibers and the creep mechanisms explained above, it is expected that the near-stoichiometric and higher purity Hi-Nicalon™ Type S fiber, which also has larger grain size, displays better creep resistance at high temperatures (>1200 °C). It has been shown that subcritical crack growth initiates in the randomly distributed flaws in Hi-Nicalon™ and Hi-Nicalon™ Type S fibers while they are loaded in air at temperatures below the creep regime threshold (<1100 °C) [14]. Slow crack growth occurs at flaws that are formed by the consumption of free carbon on the surface and at the grain boundaries of the fibers; it is further enhanced by the increase in local stresses induced by the transformation of SiC to SiO_2 near the crack tip [14]. For SiC fibers (and SiC monolithic ceramics), activation energy observations have suggested that creep-induced microcrack growth was to be the most dominant mechanism controlling fracture at the high temperatures above the creep regime threshold (>1200 °C) [15–17].

When a CMC is loaded below the matrix cracking stress, stress transfer occurs between the CMC constituents because of the mismatch in their creep resistances. This time- and temperature-dependent stress redistribution

between the fibers and the matrix and the associated creep strain evolution are best determined using unidirectional composites [18]. This has primarily been investigated by a few research groups using elastic and primary creep parameters of the fibers and matrix for various CMC systems [19–21]. Hill et al. [19] tested unidirectional SCS-6 SiC-fiber-reinforced reaction-bonded silicon nitride (RBSN) macrocomposites and estimated the stresses on the fibers and the matrix during creep at 1200 °C. They also compared experimental creep strain data with that obtained from two models: a rule of mixtures model and a finite element analysis model. Results from both models seemed close to the experimental creep strain data for short creep time (less than 25 hours). In addition, Park et al. [20] studied the creep and creep-recovery behavior of hot-pressed unidirectional SiC-fiber-reinforced Si_3N_4 matrix minicomposites at 1200 °C, where two- and three-dimensional finite element models were used to estimate creep strain behavior for hundreds of hours. Furthermore, Rugg et al. [21] tested single-fiber microcomposites (Hi-Nicalon™ or Carborundum SiC fibers coated with a chemical-vapor–deposited- (CVD-) carbon interphase and a CVD-SiC matrix) in creep at 1200 –1400 °C. Next, they estimated the evolution of stresses on the fibers and matrix in creep and the creep of uncracked single-fiber microcomposites using a simple rule of mixtures algorithm and elastic and primary creep constants, but only for less than 20 hours of creep. The above efforts utilized the elastic and primary creep parameters mostly for short creep duration where primary creep is still the most dominant creep deformation mechanism in first- and second-generation SiC fibers. This warrants further investigation to compare creep load sharing and creep strain evolutions of composites that are reinforced with second- and third-generation SiC fibers using elastic as well as primary and secondary creep parameters for long creep duration.

When a CMC is loaded with a stress above the matrix cracking stress, one or more through-thickness matrix cracks form. The stress on the fibers within the matrix crack openings increases because the matrix isn't supporting the global composite stress. If the fibers are exposed to oxidative environments, the stress on the fiber increases further because of the consumption of load-bearing fiber cross section by the various oxidation mechanisms dependent on the time, temperature, and environment. Moreover, the interaction of CMC constituents' oxidization within the crack opening can embrittle the fibers and increase the stress on the fibers [22]. For example, within a matrix crack in a $SiC_f/BN_i/SiC_m$ CMC at high temperature in air, the SiC fibers and matrix react with oxygen and form silica (SiO_2), and the boron nitride (BN) interphase reacts with oxygen and forms boria (B_2O_3) [23]. Afterwards, silica and boria react together and form a borosilicate glass melt that eventually solidifies into a glass with high SiO_2 content [23], which strongly bonds (embrittles) the fibers, fusing adjacent fibers together and

embrittling the CMC [22]. If a fiber in the strongly bonded region fails because of creep rupture crack growth or an increase in stress from oxidation, a crack can propagate through the bonded region and cause stress to transfer to the remaining crack-bridging fibers [23]. Ultimate failure occurs if the remaining fibers cannot withstand the additional increase in stress. Morscher et al. [16,24] studied the stress-rupture behavior of different precracked and pristine minicomposites (Nicalon™ and Hi-Nicalon™ fibers coated with either carbon or BN interphase with chemical-vapor-infiltrated (CVI-) SiC matrix) at 700, 950, and 1200 °C. Rupture behavior was dependent on the precrack stress, where the lower precrack stress resulted in longer rupture life.

In this investigation, pristine and precracked minicomposites with different fiber contents and types were tested in creep at a temperature of 1200 °C in air in order to determine the effects of fiber volume fraction, fiber type, and matrix damage state on minicomposite creep resistance. Hi-Nicalon™ and Hi-Nicalon™ Type S SiC-fiber-reinforced minicomposites with a BN interphase were tested with different fiber volume fractions. Precracking was done at room temperature in air based on crack density evolution data estimated from acoustic emission monitoring from a previous study of the same minicomposite batches [5]. Creep load sharing between SiC fibers and the CVI-SiC matrix was estimated using a rule-of-mixtures-based model and the constituents' elastic as well as primary and secondary creep parameters in order to identify the axial creep stress profile of each constituent in uncracked minicomposites. Tensile creep strain behavior of uncracked minicomposites with different fiber types and contents was modeled and validated for minicomposites loaded below the onset of matrix cracking. Thus, matrix cracking and associated fiber debonding were not in the scope of this modeling effort. Fracture surfaces were examined, and failure mechanisms were discussed.

2. Materials, Experimental Setup and Methodology

2.1. Materials

The minicomposite systems investigated in this paper were single-tow SiC_f/SiC minicomposites manufactured by Hyper-Therm Inc. (now Rolls Royce High Temperature Composites, RR-HTC (Cypress, CA)). They were fabricated from a single tow of SiC fibers of one of the following types: Hi-Nicalon™ (HN) (Nippon Carbon Co., Ltd.,, Tokyo, Japan) or Hi-Nicalon™ Type S (HNS) (Nippon Carbon Co., Ltd., Tokyo, Japan). The fibers were coated with a BN interphase deposited by CVI. Next, the SiC matrix was deposited by the CVI process. Various fiber contents were obtained by varying the thickness of the SiC matrix layer. The characteristics of the different fibers and CVI-SiC matrix are listed in Table 1.

The fiber, matrix, and interphase volume fractions of each specimen were determined [as in 3, 5, and 18]. The first two or three letters of each sample name correspond to its fiber type (HN or HNS), followed by *C* for pristine samples and *PC* for precracked samples, followed by the number *1*, *2* or *3* representing its fiber content (*1* is for high fiber content, *2* for intermediate, and *3* for low) and finally, the sample number.

Table 1. Characteristics of the different fibers and CVI-SiC matrix.

Constituent Type	Elastic Modulus (GPa)	Density (g/cc)	Number of Fibers per Tow	Average Fiber Diameter (μm)	Fiber Volume Fractions (%)
Hi-Nicalon™ S	400	3.1	500	12	3/16/23/43
Hi-Nicalon™	270	2.74	500	14	16/23/42
CVI-SiC Matrix	425	3.2	-	-	-

2.2. Test Specimen Preparation

The ends of the samples were placed inside slotted steel cylinders and bonded with high-temperature thermally conductive epoxy, then cured for 4 hours at 121 °C, followed by 4 hours at 176 °C. The length of the slotted steel cylinders depends on whether precracking is required for that sample (2.54 cm for pristine and 3.175 cm for precracked samples). The distance between the inner edges of the pins is 10.16 cm for pristine and 11.43 cm for precracked samples. The mounting and preparation of pristine and precracked samples were previously detailed in [3, 5, and 18].

2.3. Creep Test Design and Setup

Elevated-temperature tensile creep tests were performed using the creep test setup shown in Fig. 2. The furnace temperature profile throughout the length of the furnace was measured, and the effective gauge length of the minicomposite specimens in the hot zone was calculated, which enabled the computation of engineering strain from the recorded displacement measurements such as in [25, 26]. The strain contributions from the thermal expansion during heating and from room temperature elastic deformation of the sample and the load train were deducted from the total strain. The length on both sides of the hot zone at which the temperature drops to room temperature was neglected because creep parameters of minicomposites at the various temperatures are needed to implement the method described in [27] to accurately account for strain contribution due to the change in sample thermal profile on both sides of the hot zone.

The furnace height is 9 cm and the effective hot-zone gauge length of the minicomposite was 2.54 cm. Details about the furnace, controller, heating elements, thermocouple type, displacement sensor, and dimensions can be found in previous work [18]. The minicomposite cross-sectional area calculation is described elsewhere [3, 5]. The minicomposite stress was determined by dividing the applied load on the minicomposite by the minicomposite's average cross-sectional area. Furthermore, surfaces of uncracked minicomposites that were tested in creep were examined to verify that those samples didn't have any cracks following creep.

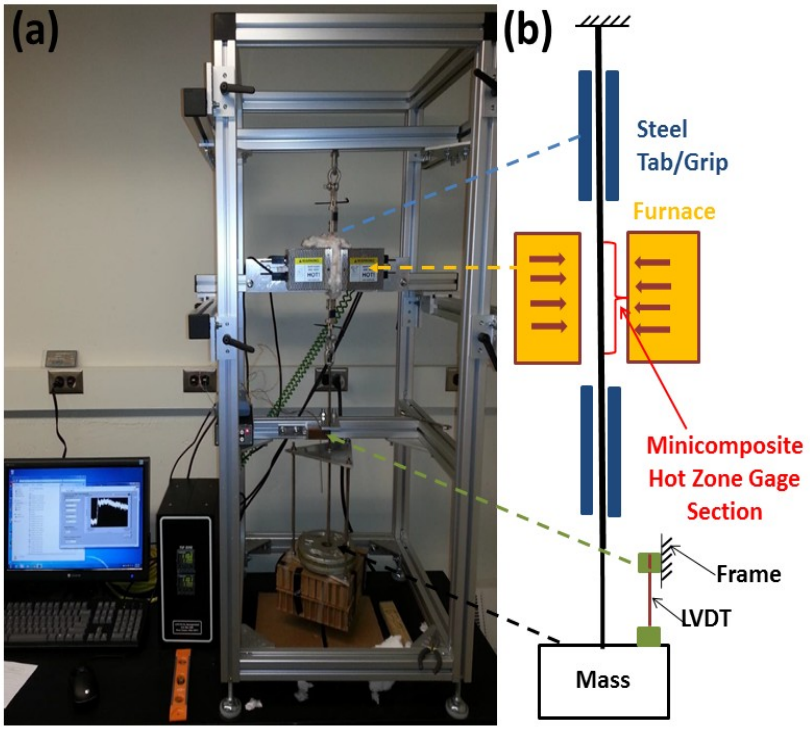

Fig. 2. (a) Image of creep experiment setup, and (b) schematic of the creep experiment.

2.4. Using AE Monitoring to Estimate Precracking Stresses

Minicomposite damage initiation and progression were monitored and characterized with the use of acoustic emission (AE) monitoring during minicomposite tensile testing at room temperature in air as in [3, 5, and 28]. The stress-dependent CVI-SiC matrix crack initiation and progression was estimated by multiplying the normalized cumulative acoustic emission energy evolution with the optically measured CVI-SiC crack density at rupture as in [3, 5, 18, and 29]. This estimate was employed to determine the precracking stress required to induce one crack per

millimeter in each minicomposite. The plot in Fig. 3a shows an example of the evolution of CVI-SiC crack density during room-temperature tensile tests as a function of minicomposite stress for HN and HNS minicomposites. The micrograph in Fig. 3b was captured using an optical microscope. It shows the induced one crack per millimeter CVI-SiC crack density in a precracked HN minicomposite. CVI-SiC cracks are delineated in Fig. 3b.

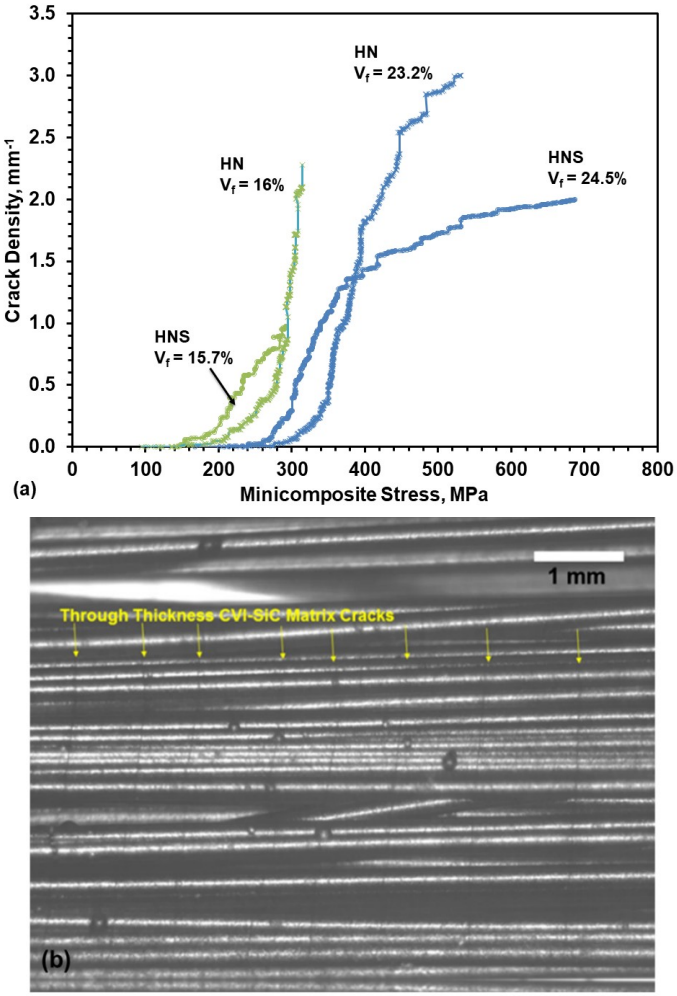

Fig. 3. (a) Stress-dependent CVI-SiC crack density evolution estimated from AE at room temperature for HN and HNS minicomposites with different fiber volume fractions. (b) Optical micrograph of precracked HN minicomposite longitudinal surface.

2.5. Post Creep Examination

Fracture surfaces and longitudinal surfaces of crept samples were examined using FEI Quanta™ 200 scanning electron microscope (SEM) with energy dispersive X-ray spectroscopy (EDS) detector that was manufactured by FEI Company (now ThermoFisher™ Scientific (Hillsboro, Oregon)). In addition, oxidation species and fiber

pullouts observed on the fracture surfaces of uncracked and precracked minicomposites that were subjected to creep for various time durations were studied.

3. Creep Behavior, Properties, and Models

3.1. Creep Behavior and Properties

Ceramic matrix minicomposites exhibit primary and secondary creep deformation stages, depending on the amount of applied stress and temperature, in addition to the initial elastic deformation that occurs upon mechanically loading the minicomposites. Fig. 4 shows a representative total strain curve for a HNS minicomposite specimen (t_{runout} = 500 hours) with high fiber content and an illustration of the regions of elastic and different creep strain.

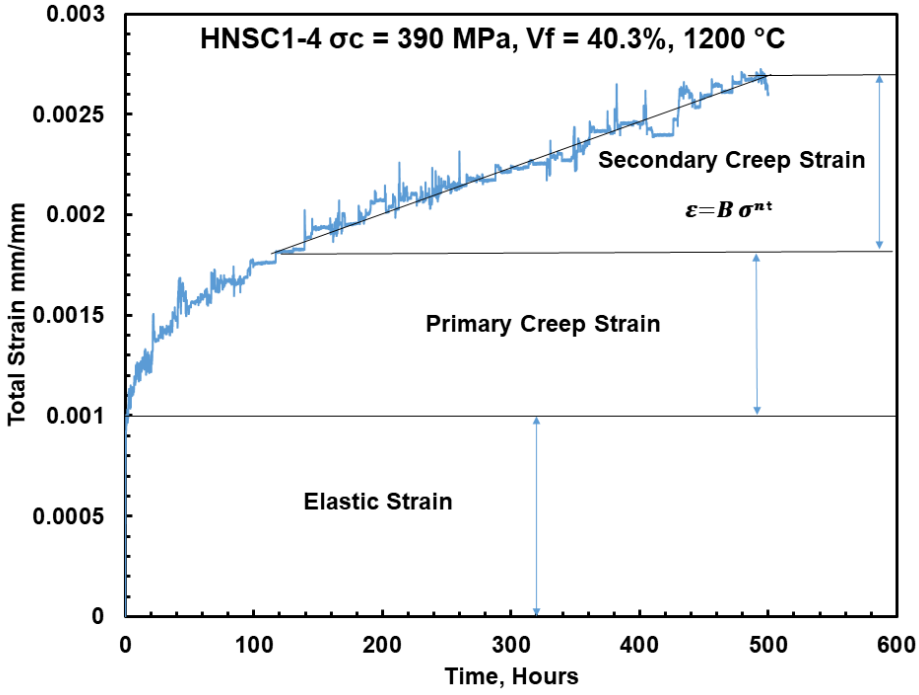

Fig. 4. Representative creep curve for HNS minicomposite with high fiber content of V_f = 40% illustrating the elastic deformation and the different creep strain regions.

In this study, tertiary creep deformation was not experimentally observed. Therefore, only elastic, primary creep, and secondary creep deformations were determined experimentally and modeled. The following well-accepted elastic and creep constitutive deformation equations were taken from Sauder et al. [12] and will be derived to calculate the axial redistribution of stress on the fibers and matrix and the strain of minicomposites with different fiber type and content in creep at 1200 °C.

$$\varepsilon_e = \frac{\sigma}{E_0} \quad (1)$$

$$\varepsilon_p = \sigma A\left[1 - e^{(-pt)}\right] \quad (2)$$

$$\varepsilon_{ss} = B\sigma^n t \quad (3)$$

$$\varepsilon = \varepsilon_e + \varepsilon_p + \varepsilon_{ss} \quad (4)$$

where subscripts *e*, *p*, and *ss* refer to the elastic deformation, primary creep deformation and steady-state creep deformation, respectively. The σ is the applied stress on the constituent (fibers or matrix) in MPa, E_0 is the elastic Young's modulus in MPa for the initial constituent (fibers or matrix), and *t* is time in seconds. Also, *A*, *B*, *n*, and *p* are creep constants for that constituent at 1200 °C. HN fiber creep constants were obtained from Sauder et al. [12] at 1200 °C. The constituents' primary and secondary creep properties are prerequisites to model and accurately obtain the evolution of load sharing between the fibers and the matrix throughout the creep tests in the load transfer model.

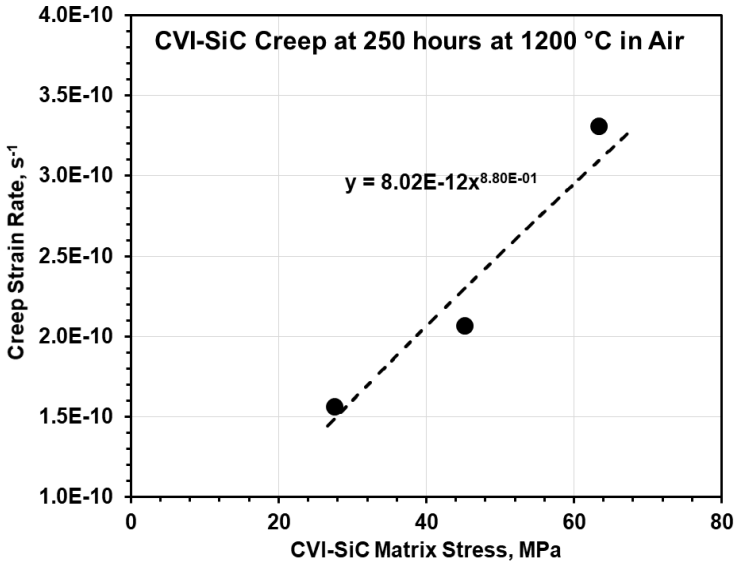

Fig. 5. Three CVI-SiC matrix tests' creep strain rates at 250 hours of creep at 1200 °C as a function of applied CVI-SiC matrix stress.

Minicomposites that have high matrix content and consist of 98% CVI-SiC and 2% Hi-Nicalon™ Type S fibers were tested in creep at 1200 °C in order to characterize the creep behavior of the CVI-SiC matrix separately for a duration over 1350 hours. Those samples were treated as pure 100% CVI-SiC. CVI-SiC creep stress exponent *n* and steady-state creep parameter *B* were obtained using two methods. In the first method, three different CVI-SiC

samples (98% matrix content minicomposites) were creep tested at three different stresses at 1200 °C. Fig. 5 shows those specimens' creep strain rate at 250 hours of creep at 1200 °C as a function of applied CVI-SiC stress. The plotted slope in Fig. 5 gives a 0.88 value for the stress exponent (n) and 8.02×10^{-12} value for the steady-state creep parameter (B) for CVI-SiC.

In the second method, a stress exponent value of 1.05 for CVI-SiC was obtained from fitting Eq. (3) using the last 700 hours of creep data from CVI-SiC that was tested in creep under 69 MPa stress at 1200 °C for over 1350 hours in Fig. 6a; this seems to be very close to the CVI-SiC stress exponent value of 1 that was well accepted in previous research by Lamon et al. [30]. Afterwards, n was set to be 1 and the CVI-SiC creep curve was fitted with Eq. (4) to produce the values of primary creep constants A and p and secondary creep constant B. Fig. 6a shows a CVI-SiC specimen creep curve with the best curve fit that was used to get the CVI-SiC creep constants. It should be noted that creep data in this curve that were between 200 and 560 hours were excluded because of data acquisition noise during that time range in order to get high-fidelity CVI-SiC creep constants. Secondary creep parameters (n, B) that were obtained from both methods are within the same order of magnitude, but they were sensitive to the duration of creep tests at which they were extracted. Since the stress exponent that was obtained from the second method is in agreement with what was reported in literature [30], all creep parameters that were obtained from this method were used in the modeling efforts in the present study.

HNS fiber creep parameters were obtained experimentally by testing single HNS fiber samples in creep at 1200 °C in vacuum (pressure ~10^{-4} Pa) and fitting Eq. (4) to the data. A schematic and procedure for the single-fiber creep test can be found in [31 and 32]. Fig. 6b shows two single HNS fiber creep curves with creep model prediction using best fit HNS fiber creep parameters. Primary and secondary creep constants for HN fibers, HNS fibers and CVI-SiC matrix are shown in Table 2.

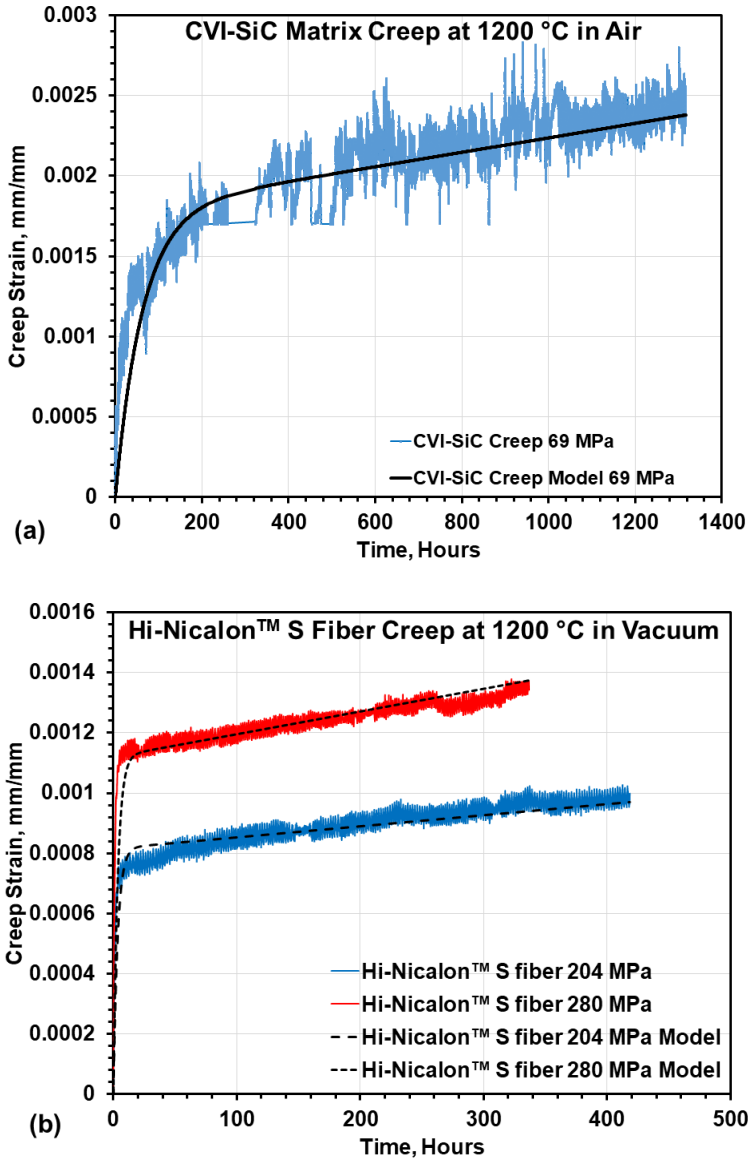

Fig. 6. (a) CVI-SiC specimen creep curve at 1200 °C in air under a stress of 69 MPa with creep model prediction using best fit CVI-SiC matrix creep parameters and (b) HNS single fiber creep with creep model prediction using best fit HNS fiber creep parameters.

Table 2. Creep constants for HN and HNS fibers and CVI-SiC matrix at 1200 °C.

Constituent	*A* (1/MPa)	*P* (s^{-1})	*B* (s^{-1}/MPa)	*n* (Stress exponent)
Hi-Nicalon™ [12]	2.127×10^{-5}	1.485×10^{-5}	1.77×10^{-15}	2.3
Hi-Nicalon™ S	4×10^{-6}	8×10^{-5}	6×10^{-16}	2.265
CVI-SiC Matrix	2.59×10^{-5}	4.432×10^{-6}	1.81×10^{-12}	1

3.2. Fibers and Matrix Creep Load Sharing Model

In ceramic matrix minicomposites, creep deformation is controlled by the slowest creep mechanism of the slowest creep constituent. This causes the load to be transferred from the constituent that creeps the fastest to the constituent that creeps the slowest. In other words, when a minicomposite is loaded with a specific global composite mechanical load at high temperature, the constituent that has the higher creep strain rate will shed load to the constituent that has the lower creep strain rate. This increase in the load on the most creep-resistant constituent will directly affect the elastic deformation and the creep deformation evolution. This occurs mostly in the primary creep deformation stage, which is known to be where the majority of load transfer occurs between the constituents. Therefore, a rule-of-mixtures-based method was used to obtain the redistribution of stresses on the fibers and matrix during creep with the assumption that all fibers within the single-tow minicomposite are homogeneously loaded and perfectly parallel.

In this method, Eq. (4) was expanded to represent total creep strain to include elastic, primary, and secondary creep components for the fibers and the matrix in Eqs. (5) and (6), respectively. Next, it was assumed that the strain of the fibers and matrix are equal, and the strain rate of them are equal, at any given time during the creep tests of pristine minicomposites. This is stated below in Eq. (7) for the isostrain condition and in Eq. (8) for the isostrain rate condition. Afterwards, Eqs. (5) and (6) were derived with respect to time as shown below in Eqs. (9) and (10) for the fibers and the matrix, respectively. Also, the rule of mixtures was used to substitute for the matrix stress rate as shown in Eq. (11) and solve the derived equation for the stress rate on the fiber. Minicomposite global stress does not change with time, and thus the minicomposites' stress rate has a value of zero as seen in Eq. (12). Finally, the resulting derived stress rates on the fibers and matrix are shown in Eqs. (13) and (14), respectively.

$$\varepsilon_f = \frac{\sigma_f}{E_f} + \sigma_f A_f ¿ \quad (5)$$

$$\varepsilon_m = \frac{\sigma_m}{E_m} + \sigma_m A_m ¿ \quad (6)$$

$$\varepsilon_f = \varepsilon_m \quad (7)$$

$$\dot{\varepsilon_f} = \dot{\varepsilon_m} \quad (8)$$

$$\dot{\varepsilon_f} = \frac{\dot{\sigma_f}}{E_f} + \dot{\sigma_f} A_f - \dot{\sigma_f} A_f e^{(-P¿¿ft) + \sigma_f A_f P_f ¿¿} \quad (9)$$

$$\dot{\varepsilon_m} = \frac{\dot{\sigma_m}}{E_m} + \dot{\sigma_m} A_m - \dot{\sigma_m} A_m e^{(-P¿¿mt) + \sigma_m A_m P_m ¿¿} \quad (10)$$

$$\dot{\sigma_m} = \frac{\dot{\sigma} - \dot{\sigma_f} V_f}{V_m} \quad (11)$$

$$\dot{\sigma} = 0 \quad (12)$$

$$\dot{\sigma_f} = \sigma_m A_m P_m ¿¿ \quad (13)$$

$$\dot{\sigma_m} = \sigma_f A_f P_f ¿¿ \quad (14)$$

The initial stresses on the fibers and the matrix upon loading the minicomposites at time zero were calculated using Eqs. (15) and (16), respectively.

$$\sigma_{f(t=0)} = \frac{\sigma_c E_f}{E_C} \quad (15)$$

$$\sigma_{m(t=0)} = \frac{\sigma_{f(t=0)} E_{eff-Mat}}{E_f} \quad (16)$$

Where $E_{eff-Mat} = \frac{E_c - V_f E_f}{V_m}$, E_c is the minicomposite modulus, E_f the fiber modulus, and $E_{eff\text{-}Mat}$ the effective matrix modulus. The σ_c is the minicomposite stress, σ_f is the stress on the fibers, and σ_m is the stress on the matrix [33]. Next, the rest of the stress profiles on the fibers and the matrix in creep were calculated using Eq. (17) for the fibers and Eq. (18) for the matrix.

$$\sigma_{f(i)} = \sigma_{f(i-1)} + \Delta t \dot{\sigma}_{f(i-1)} \quad (17)$$

$$\sigma_{m(i)} = \sigma_{m(i-1)} + \Delta t \dot{\sigma}_{m(i-1)} \quad (18)$$

with $\Delta t = t_i - t_{i-1}$ = 10 seconds

3.3. Creep Strain Evolution Model

The minicomposites' creep strain evolution is expected to be controlled by load transfer between the composites' constituents (i.e., fibers and matrix). This is due to the creep resistance differential or mismatch between the fibers and the matrix. Also, creep evolution is greatly affected by thermomechanical loading histories.

Therefore, a creep model of a ceramic matrix minicomposite should account for the loading history of the composite that is being modeled. In this work, the creep strain evolution model was constructed and developed for ceramic matrix minicomposites having different fiber types and volume fractions and with different loading histories. The model assumes that a minicomposite is loaded with a stress below the stress at the onset of CVI-SiC matrix cracking, where no cracks are expected to form. The model assumes instantaneous loading, perfectly parallel fibers within the tow with homogenous loading, ideal load transfer across the BN interface, and no thermal residual stresses. It also assumes equal fiber and matrix creep strain (isostrain). It calculates the evolution of fiber creep strain as a function of stress redistribution between the fibers and the matrix in creep and as a function of fiber creep loading histories. Initial fiber elastic and creep strain ε_1 is obtained using fiber creep strain Eq. (5) at a 10-second time increment (t_1 = 10 seconds) and at the initial fiber stress (σ_1) that was obtained from the rule of mixtures with the use of the fiber and matrix primary and secondary creep parameters that were obtained from Table 2. Afterward, the stress change rate on the fibers and matrix was calculated using the stress change model in Eqs. (13) and (14), respectively. The new stress on the fibers (σ_2) and on the matrix was then calculated (at t_1 = 10 seconds) using the load transfer model in Eqs. (17) and (18), respectively. Next, the modified secant numerical method was used to solve the nonlinear Eq. (20) for the relative time (t^*_2) that it took the fibers at higher stress level (σ_2) to induce fiber creep strain of ε_1. Then, a 10-second time step was added to the relative time and substituted into Eq. (24) along with σ_2 and the fiber primary and secondary creep parameters from Table 2 to obtain fiber creep strain at σ_2 as if it were under this stress from the beginning of the test. Similarly, the model calculates relative creep time at each fiber stress increase, due to load sharing, and adds a 10second time step to the relative creep time to calculate the evolution of creep. Fig. 7 shows an illustration of this creep model methodology.

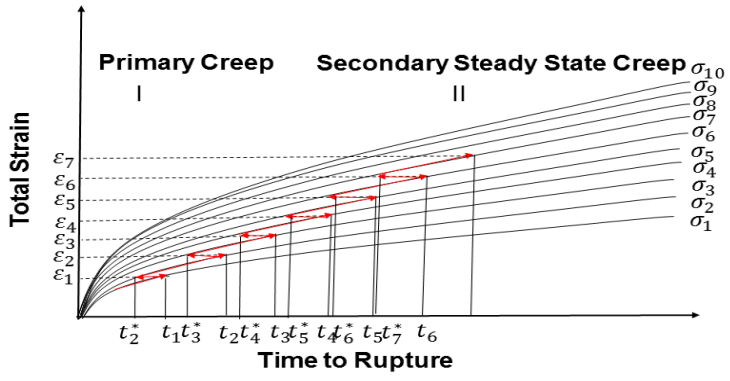

Fig. 7. Creep model methodology illustration.

Equations (19) to (23) show details of the procedure of a secant numerical method that was used to back out a relative time value t^* when everything else was known in Eq. (20).

$$\varepsilon_f(t_i)=\frac{\sigma_f}{E_f}+\sigma_f A_f\left[1-e^{-P_f t_i}\right]+B_f \sigma_f^{n_f} t_i \quad (19)$$

$$\varepsilon_f(t_i)-\frac{\sigma_f}{E_f}-\sigma_f A_f\left[1-e^{-P_f t_i}\right]-B_f \sigma_f^{n_f} t_i=0 \quad (20)$$

$$t_{i+1}^{¿}=t_i-\frac{\varepsilon_f(t_i)}{\varepsilon_f^{'}(t_i)} \quad (21)$$

$$\varepsilon_f^{'}(t_i)=\frac{\varepsilon_f(t_i)-\varepsilon_f(t_{i-1}^{¿})}{t_i-t_{i-1}^{¿}} \quad (22)$$

$$t_{i+1}^{¿}=t_i-\frac{\Delta * \varepsilon_f(t_i)}{\varepsilon_f(t_i)-\varepsilon_f(t_{i-1}^{¿})} \quad (23)$$

with $\Delta=t_i-t_{i-1}^{¿}= 10^{-8}$ s

$$\varepsilon_{fi}(10+t_{i+1}^{¿})=\frac{\sigma_{fi}}{E_f}+\sigma_{fi} A_f\left[1-e^{-P_f(10+t_{i+1}^{¿})}\right]+B_f \sigma_{fi}^{n_f}(10+t_{i+1}^{¿}) \quad (24)$$

Up to 13 iterative loops were performed for calculating each relative time value at the calculated fiber stress and strain values in order to eliminate the errors. Afterwards, a 10-second time step was added to the relative creep time at each fiber stress increase step, then substituted in Eq. (24) to calculate the true evolution of creep.

4. Results and Discussion

4.1. Creep Damage Evolution

The evolution of the creep strain as a function of time to rupture is shown in Fig. 8a for tensile creep tests at 1200 °C in air of one specimen from each fiber type with the same CVI-SiC matrix and fiber content. Clearly, the minicomposite that is reinforced with HNS fibers is the most creep resistant minicomposite (having lower creep strain rate, less total strain at a given time and stress, and longer time to rupture under similar or more severe loading conditions). In comparison, the minicomposite that is reinforced with HN fibers in Fig. 8a exhibits higher creep strain, strain rate, and total strain as well as a slightly shorter time to rupture. The difference in creep and creep rupture behavior between the two minicomposites is due to the difference in creep resistances and creep rupture of

HNS and HN fibers, since both minicomposites have similar fiber content and matrix type. The HN fiber microstructure consists of small SiC grains with an excess of free carbon, whereas HNS fibers have a polycrystalline microstructure with larger grain size and contain less excess carbon and oxygen. Thus, HNS fibers have superior creep behavior [9–15]. Fig. 8b shows the creep behavior of as-received (uncracked) and precracked HN fiber-reinforced minicomposites as a function of time. It implies that the precracked minicomposite has greater creep strain and strain rates and shorter time to rupture, which is because of several reasons. First, longer lengths of fibers are subjected to higher stress along the opening of CVI-SiC matrix cracks in the precracked specimen, which failed earlier than the uncracked specimen. Conversely, the fibers are not fully loaded in the intact uncracked HN minicomposite where the matrix carries some load, and the stress on the fibers is a fraction of that on the fibers in the precracked case. Second, the oxidation of the BN interphase, CVI-SiC matrix, and HN fibers in the vicinity of matrix cracks in the precracked specimen leads to a high degree of environmental degradation. This causes fiber embrittlement and the loss of fiber load-bearing capacity, which can increase creep strain and strain rate and shorten the life of the precracked specimen. The effects of oxidation in precracked specimens are discussed in the post-creep-fracture surface SEM analysis in section 4.4.

Fig. 8. Representative creep curves of (a) as-received HN and HNS fiber-reinforced minicomposites and (b) as-received and precracked HN minicomposites.

Fig. 9 shows the experimental creep strain evolution in air at 1200 °C as a function of time for uncracked HN and HNS fiber-reinforced minicomposites with different fiber contents under load. In general, creep strain and strain rates increased with the increase in applied stress in both HN and HNS minicomposites. Similarly, creep strain and strain rates increased with the increase in fiber volume fraction when minicomposites with the same fiber type are subjected to the same load because minicomposites with higher fiber content have less matrix area to carry load. In order to understand the effect of fiber volume fraction on the creep of uncracked minicomposites, it is most relevant to compare creep curves of minicomposites that have the same fiber type and the same minicomposite stress with

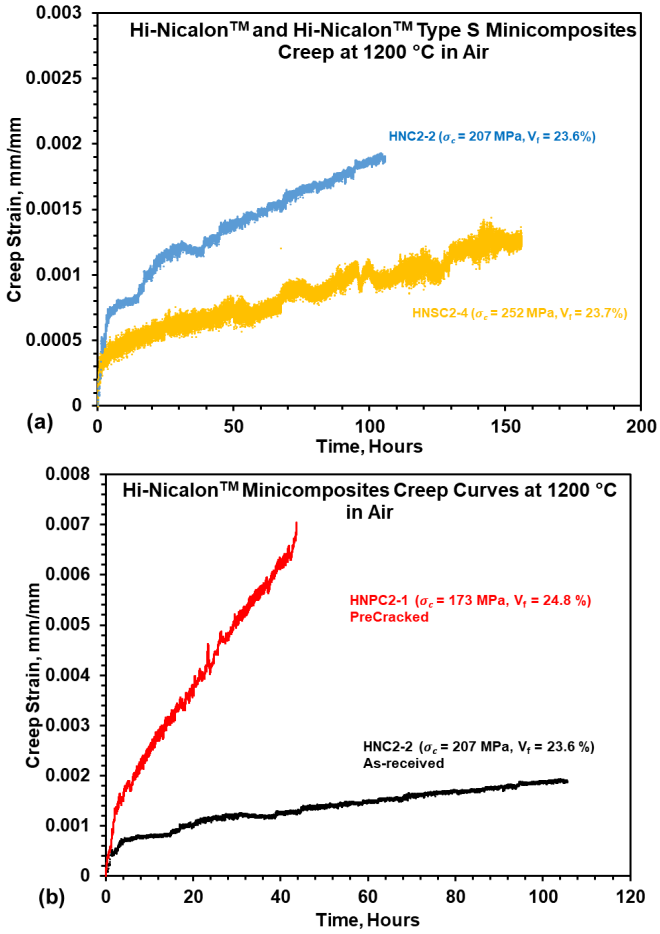

different fiber contents. However, available creep data in Fig. 9 is utilized here to extract the influence of fiber content on creep behavior of minicomposites although there are some variations in mincomposite stresses in addition to the variation in fiber contents. For instance, overall creep resistance and rupture of uncracked specimen

HNC2-3 (σ_c = 199 MPa, V_f = 25.5%) is better than that of HNC3-2 (σ_c = 187 MPa, V_f = 20.8%) in Fig. 9a even though the stress on HNC2-3 is slightly higher. In that case, the increase in HN fiber volume fraction improves the creep durability (creep resistance and rupture life) of the uncracked minicomposites. Notably, a similar trend is observed more clearly in uncracked HNS specimens in Fig. 9b. For example, creep strain and creep strain rate of uncracked specimens HNSC1-1 (σ_c = 397 MPa, V_f = 37.3%) and HNSC1-2 (σ_c = 365 MPa, V_f = 35.3%) are greater than that of specimen HNSC1-4 (σ_c = 390 MPa, V_f = 40.3%), which contains higher fiber content and didn't fail in Fig. 9b. This indicates that the increase in HNS fiber volume fraction enhances the creep durability of the uncracked minicomposites as well. The observed influence of fiber content on creep resistance agrees with the primary and secondary creep parameters of the different SiC fibers and CVI-SiC matrix that are summarized in Table 2, and this is further examined in the creep modeling section 4.3.

As shown in Fig. 10, precracked HN and HNS minicomposites with similar fiber contents exhibit higher creep strain rates than pristine (uncracked) samples when compared as a function of fiber stress if fully loaded (σ_c/V_f). This is due to longer lengths of fibers being exposed to higher stress within the CVI-SiC matrix cracks and the oxidation of the interphase and fibers that occurs in precracked samples. In uncracked samples, the CVI-SiC matrix carries more stress via load sharing and provides the fibers with oxidation protection. Those trends have been reported for different minicomposite systems earlier in the literature [22].

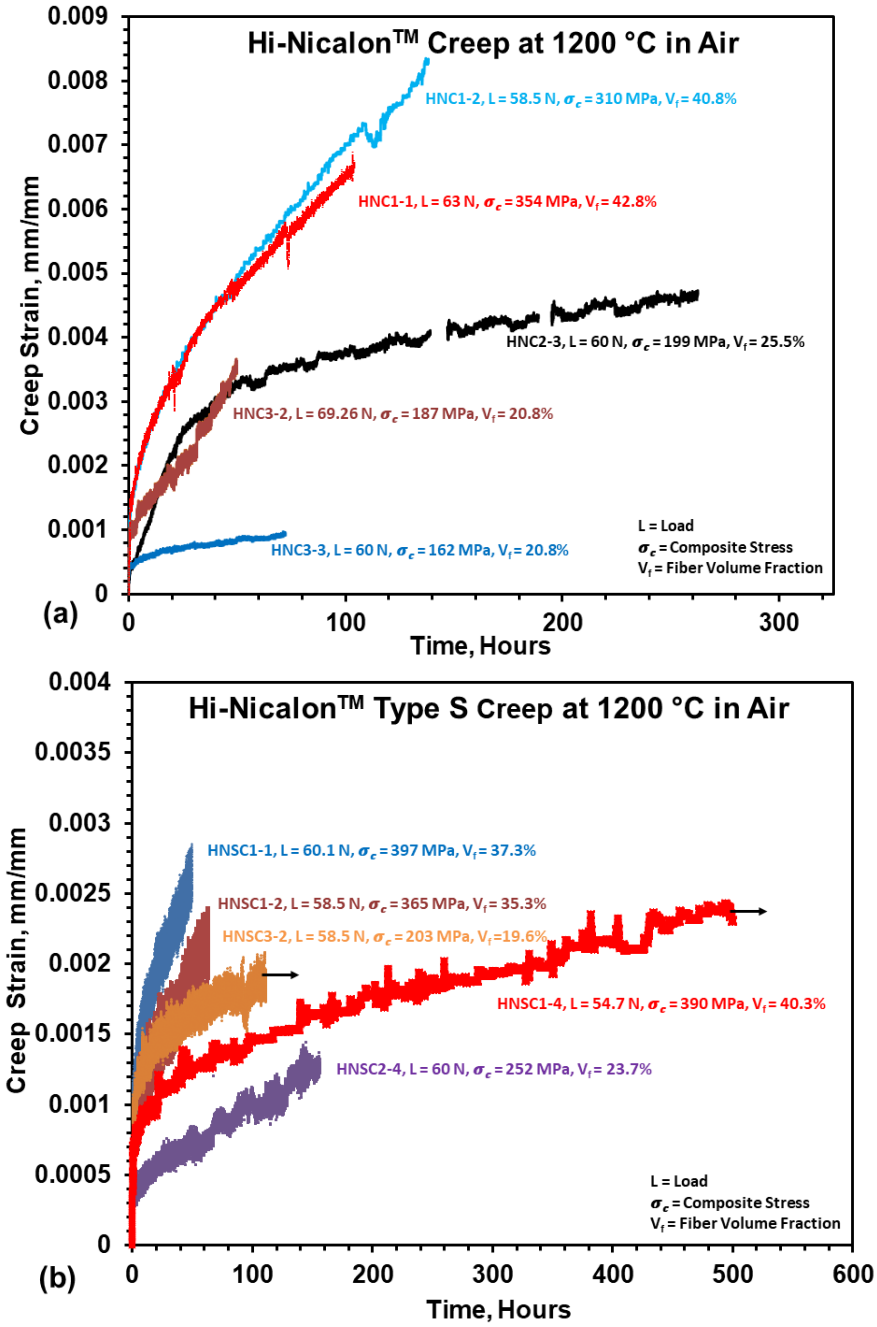

Fig. 9. Experimental creep curves in air at 1200 °C for (a) HN minicomposites with different fiber contents under similar stress on fibers if fully loaded and (b) HNS minicomposites with different fiber contents under different stresses on the fibers.

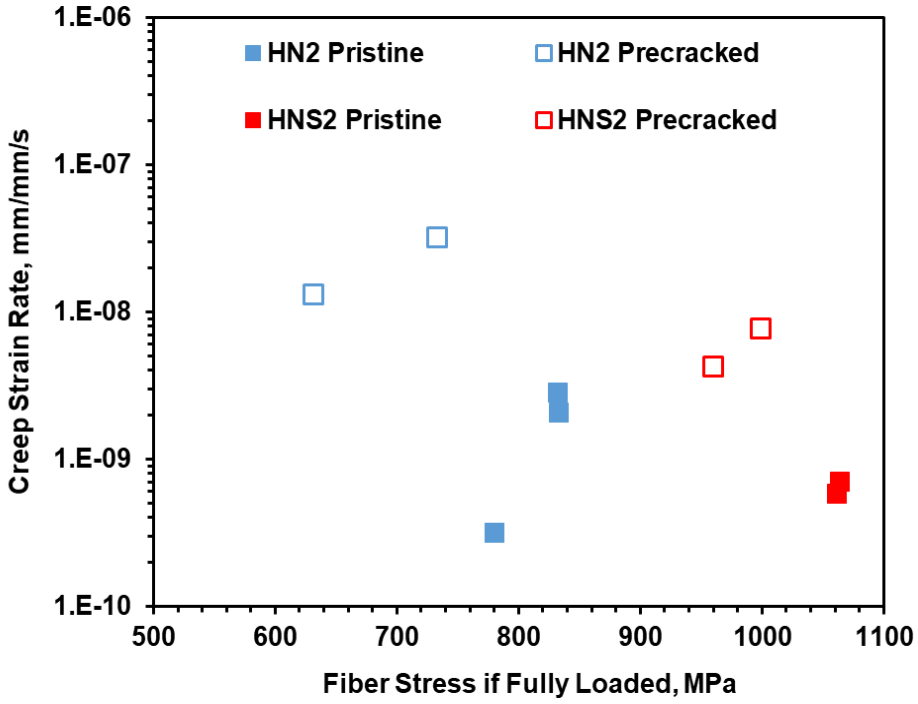

Fig. 10. Comparison of creep strain rates of precracked and pristine HN and HNS minicomposites.

4.2. Load Transfer in Creep

Primary and steady-state creep contributions were considered in the model developed for obtaining stress redistribution between the fibers and the matrix. Stress rate was calculated using Eqs. (13) and (14) for fibers and CVI-SiC matrix, respectively, for three minicomposites with different fiber contents under the same minicomposites global stress of 199 MPa at 1200 °C in air. Stress rates were plotted as a function of time in hours for HN and HNS minicomposites in Figs. 11a and 11c, respectively. Those stress rates were then used in Eqs. (17) and (18) in order to calculate the axial stress on the SiC fibers and the CVI-SiC matrix during creep. The axial stresses for three HN minicomposites with different fiber volume fractions were plotted as a function of time in hours as seen in Fig. 11b, which shows that most of the load transfer occurs in the primary creep region before reaching 130 hours of creep at 1200 °C. The initial stress on HN fibers and CVI-SiC matrix is not equal. CVI-SiC has a higher elastic modulus than that of the HN fibers. Therefore, the initial stress on the matrix is higher than that on the Hi-Nicalon™ fibers. This behavior was observed in previous work [21] for short time (<20 hours) by only using HN fiber and CVI-SiC primary creep parameters.

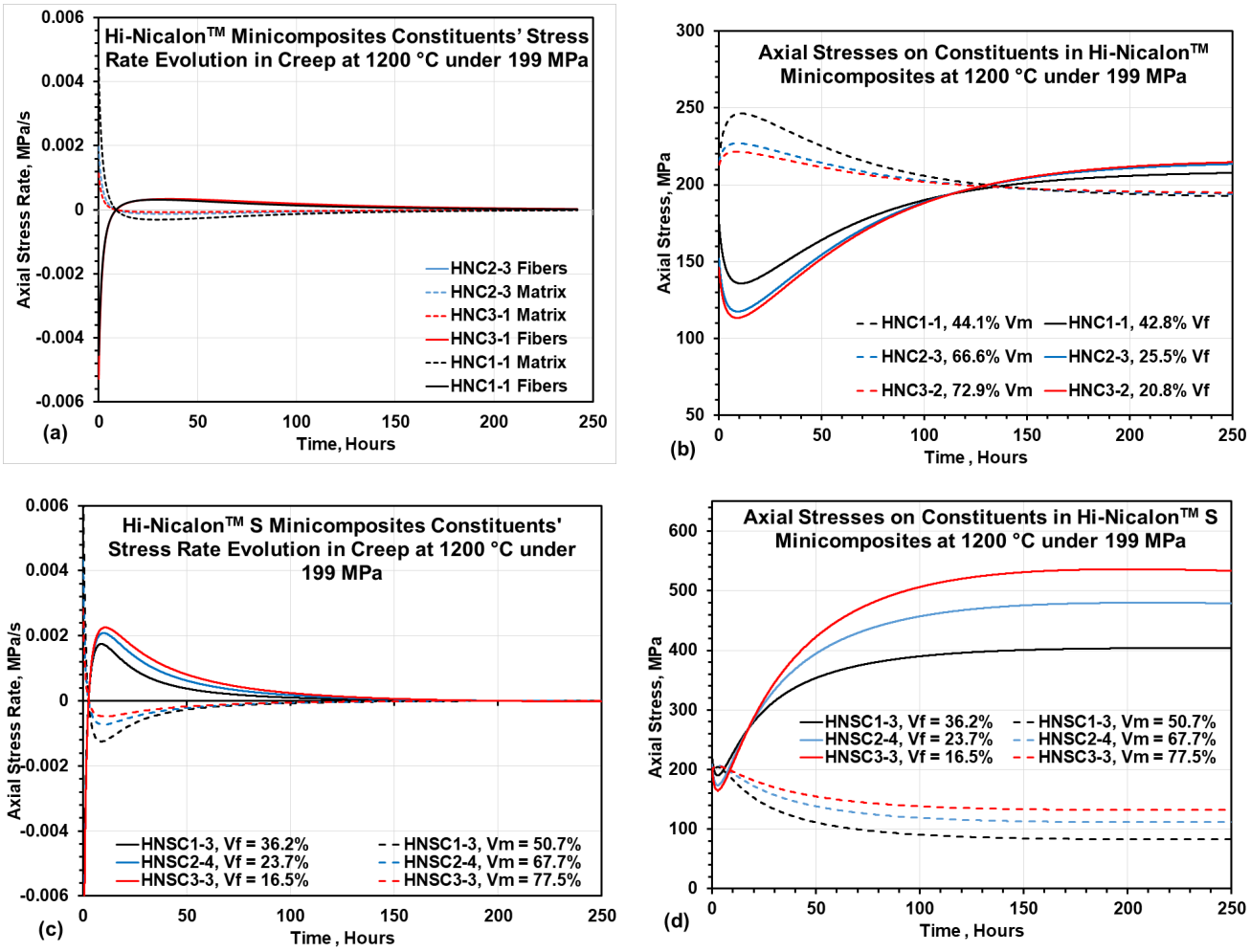

Fig. 11. (a) Stress rate evolutions and (b) corresponding axial stress profiles of HN fibers and CVI-SiC matrix for three pristine HN minicomposites with V_f = 42.8%, 25.5%, and 20.8%;. and (c) stress rate evolutions and (d) resulting axial stress profiles of HNS fibers and CVI-SiC matrix for three pristine HNS minicomposites with V_f = 36.2%, 23.7%, and 16.5%, in creep at 1200 °C in air under σ_c = 199 MPa global minicomposite stress.

The initial increase in stress on the matrices in Figs. 11b and 11d during the first few hours of creep is due to the elastic modulus mismatch between the fiber and the matrix. In addition, it is caused by the difference between the fiber's and matrix's grain sizes and impurities at grain boundaries resulting in a mismatch in the fiber's and matrix's grain realignments and grain boundary diffusion during the primary creep region. Fig. 11d shows that the stresses on HNS fibers and CVI-SiC start out equal since the fibers and matrix have similar elastic moduli. It also shows that CVI-SiC matrix is shedding load to the HNS fibers rapidly during primary creep. Load shedding slows down after 100 hours in creep as the minicomposite secondary creep mechanism becomes more dominant, where the stress on each constituent becomes constant. It is worth mentioning that the fibers start carrying more stress than the matrix at

a crossover time of 130 hours for HN fibers and 25 hours for HNS fibers. Those crossover points are consistent with the end of primary creep regime in HN fibers in [12] and HNS fibers in Fig. 6b at 1200 °C. Moreover, it was observed that HNS fibers are clearly more creep resistant than HN fibers by comparing fiber and matrix load sharing for HN and HNS minicomposites under the same loading conditions in Figs. 11b and 11d, respectively. This stress transfer model has the advantage of predicting the continuous redistribution of the stresses on the fibers and the matrix throughout the creep test, depending on the fibers' and the matrix's primary and secondary creep properties. Furthermore, it was used to predict axial stress redistribution on the fibers and matrix when in creep at 1200 °C for different minicomposite stresses and fiber volume fractions. The stress redistribution results in Figs. 11b and 11d will be used in the next section to model minicomposites creep strain evolution.

4.3. Creep Model Results

In order to study the influence of fiber content on the creep of minicomposites, relative fiber creep time evolutions of minicomposites with the same fiber type and minicomposite stress (199 MPa) with various fiber contents are compared in Figs. 12a and 12c, for HN and HNS, respectively. Next, the evolutions of relative fiber creep time were used to calculate the associated creep strain evolutions of minicomposites in Figs. 12b and 12d, for HN and HNS, respectively. For both fiber types, minicomposites have the lowest creep strain value when relative fiber creep time is greatest at a certain time and minicomposite stress. This is because the relative fiber creep time is inversely proportional to the stress on the fibers at any given time when the minicomposites are loaded with the same global stress. Consequently, the constituent (fibers or matrix) that carries more stress is the more creep resistant constituent at any given point in the modeled creep curves in Figs. 12b and 12d. Clearly, CVI-SiC matrix is more creep resistant than HN fibers for the first 130 hours and more creep resistant than HNS fibers up to 25 hours in creep at 1200 °C. Further, the HN minicomposite with the highest fiber content is the most creep resistant minicomposite beyond 130 hours of creep in Fig 12b. This indicates that HN fibers are more creep resistant than CVI-SiC and under more stress after 130 in creep. This is due to matrix relaxation as primary creep of the matrix decreases and steady-state creep becomes more significant. The HNS minicomposite with the highest fiber content is the most creep resistant minicomposite after the first 25 hours of creep in Fig 12d. This implies that HNS fibers are more creep resistant than CVI-SiC while carrying more load starting as early as 25 hours into the creep test. In addition, this suggests that HNS fibers are more creep resistant than HN fibers since HNS fibers start carrying more load than CVI-SiC much earlier than HN fibers. This is due to fact that the fibers of both types and matrix all creep

differently in primary and secondary regimes. However, load sharing is time and temperature dependent, so the direction of load shedding will change depending on the creep test temperature and the time at which the primary creep regime of each separate constituent slows down. This creep model generated representative trends and predicted the relative difference in creep behavior of the minicomposites reinforced with two different fiber types and with various fiber volume fractions. The trends in the results from this creep model are in good agreement with the actual measured creep strain evolutions that are shown in Fig. 9.

Relative fiber creep time (Fig. 12e) and the resulting creep strain evolutions (Fig. 12f) were calculated to understand the combined effect of varying the HN minicomposite stress (354, 199, and 186 MPa) and fiber content (42.8%, 25.5%, and 20.8%) on the creep strain evolution. The results in Fig. 12f demonstrate an increase in creep strain and strain rate with the increase in applied minicomposite stress and fiber content. A relatively similar trend is observed in experimental creep curves of HN minicomposites in Fig. 9a, and it is expected to be the same for HNS minicomposites in Fig. 9b.

Experimental creep strain evolution was compared to creep strain model evolution for HN and HNS minicomposites in Fig. 13. It shows good overall agreement between experimental results and model prediction of creep strain evolution for minicomposites of different fiber type and content under stresses below the onset of CVI-SiC matrix cracking stresses. Some variation between model and experimental data may be due to the model assumptions of perfectly parallel fibers within the tow with homogenous loading and ideal load transfer across the BN interface. However, in reality there is a random distribution of porosity and flaw sizes and shapes in minicomposites that will change the local effective fiber content, fiber alignment, and cross-sectional area and thus will affect load sharing and creep evolution behavior. Those factors may change the time- and temperature-dependent load-sharing and axial stresses on the fibers and matrix. Moreover, this model will not be able to predict creep strain evolution of cracked minicomposites because this model is constructed for uncracked minicomposite systems. So, if any matrix cracks were to form upon mechanically loading the minicomposites or during creep, the model will not account for or capture the additional local creep strain in the vicinity of CVI-SiC matrix cracks. Surfaces of samples in Fig. 13 were examined, and no cracks in the CVI-SiC were observed. This bottom-up model approach can also be used to generate predictions of creep strain evolution of different minicomposites that are manufactured from different constituents (i.e., fiber type and matrix type) by only using the different constituents' creep parameters. That is a beneficial tool for use as part of characterization and screening while improving and

developing new processing techniques or new constituents with enhanced thermomechanical properties and creep resistance.

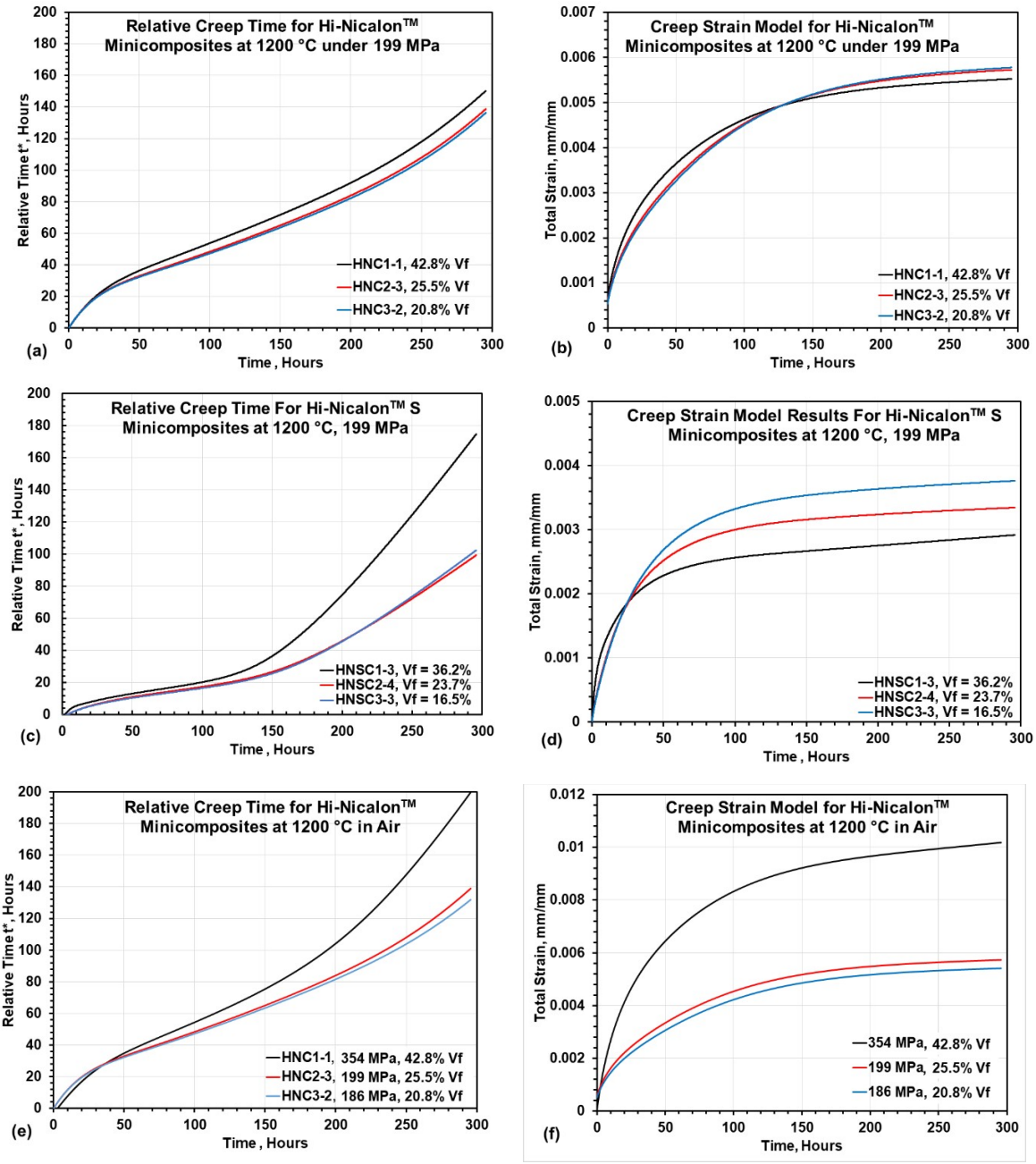

Fig. 12. (a) Relative fiber creep time and (b) associated creep strain model results for three pristine HN minicomposites with V_f = 42.8%, 25.5%, and 20.8% under σ_c = 199 MPa; (c) relative fiber creep time and (d) associated creep strain model results for three pristine HNS minicomposites with V_f = 36.2%, 23.7%, and 16.5 % under σ_c =199 MPa; and (e) relative fiber creep time and (f) associated creep strain model results for three pristine HN minicomposites with V_f = 42.8%, 25.5%, and 20.8% loaded with different minicomposite stresses σ_c = 354, 199, and 186 MPa, respectively, in air at 1200 °C.

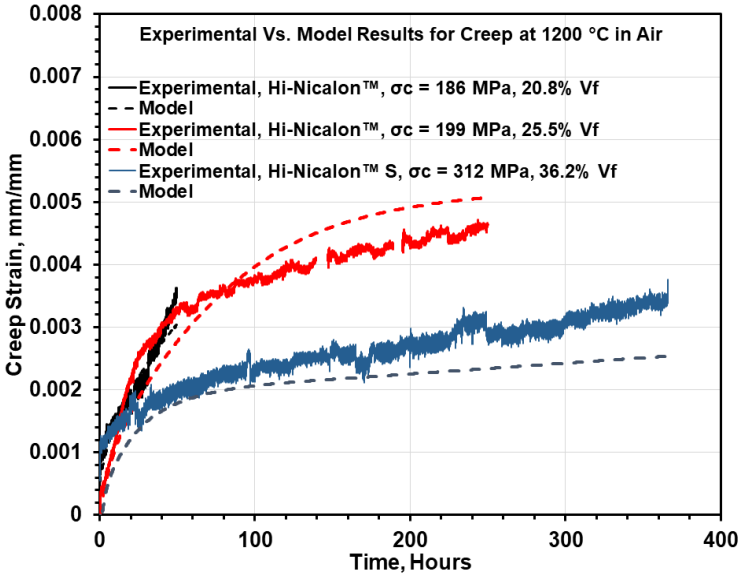

Fig. 13. Experimental creep strain evolution and modeled creep strain evolution for HN and HNS minicomposites with different fiber contents under different minicomposite stresses at 1200 °C in air.

Currently, this creep model does not predict failure times. However, the results from stress transfer and creep strain models can be used to help construct an envelope with lower and upper bounds for creep rupture life of uncracked composites that are loaded below the matrix cracking stress. A lower bound (minimum time to rupture) can be established by incorporating the modeled evolutions of stresses on the fibers and matrix in creep rupture life models to accurately estimate the probability of failure and time to rupture. Several creep rupture models are reviewed in [34]. An upper bound (maximum time to rupture) can be constructed by using a known high-temperature average strain to failure to identify the time at which the composite reaches that strain in the creep strain model results.

4.4. Post Creep SEM

Creep-rupture was established to be the failure mechanism of HN/BN/CVI-SiC minicomposites [16] and failure mechanism of monolithic ceramics and HN and HNS fibers [17] in air at 1200 °C. Furthermore, slow crack growth has been shown to be the leading failure mechanism of monolithic ceramics and of HN and HNS fibers in air at temperatures below 1100 °C [14]. Therefore, a fiber or matrix creep-rupture-controlled degradation mechanism was proposed here to be the primary failure mechanism of pristine minicomposites that were tested in creep at a stress below the matrix cracking stress. Fracture surfaces of crept pristine samples are shown in Figs. 14a to 14e where no

fiber oxidation. Significant fiber pullouts are evidenced in the fracture surface of pristine specimen HNSC1-3 (Figs. 14a, 14b, and 14e), which had failed after 366 hours, and in the fracture surface of pristine specimen HNC3-1 (Figs. 14c and 14d), which had failed after 404 hours, in creep. This shows that internal oxidation did not contribute to creep-rupture in pristine samples and either the fibers or the matrix failed solely due to creep-rupture only. In contrast, little to no fiber pullout was observed on the fracture surface of precracked specimen HNSPC2-1 (V_f = 25.7%, σ_c = 247 MPa, 1200 °C) in Fig. 14f. It failed after 91 hours, indicating brittle fracture due to strong fiber to matrix bonding from oxidation along with fiber embrittlement in the vicinity of CVI-SiC matrix through-thickness

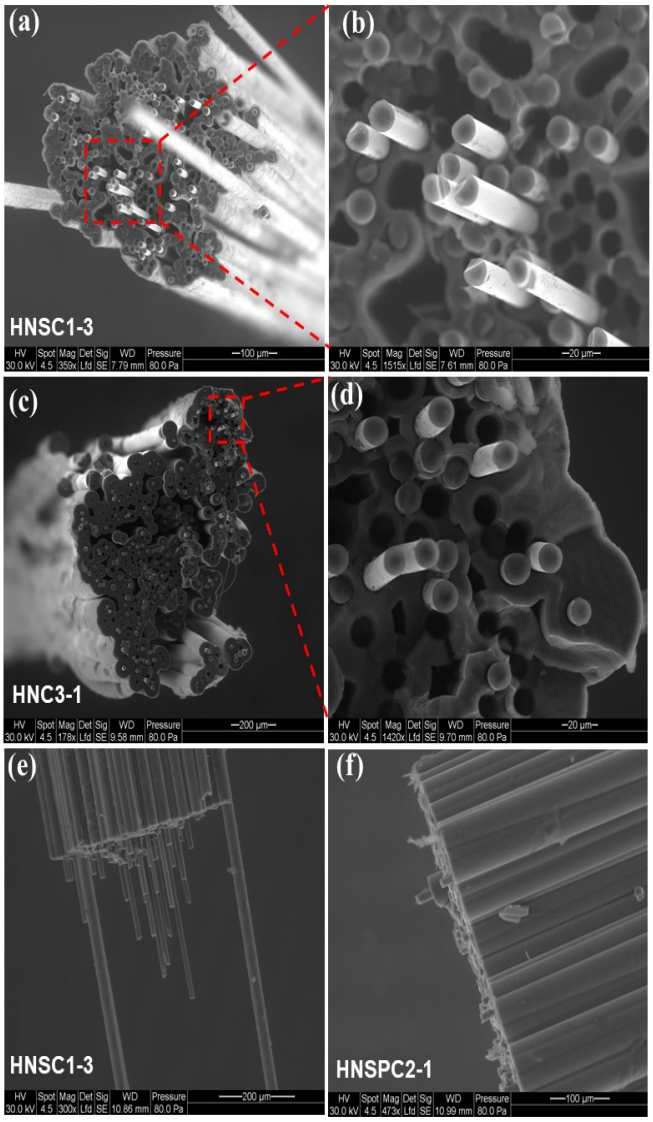

cracks.

Fig. 14. SEM images of (a) low magnification and (b) high magnification of fracture surface of pristine HNS minicomposite specimen HNSC1-3 (V_f = 36.2 %, σ_c = 312 MPa, and $t_{rupture}$ = 366 hours), (c) low magnification and (d) high magnification of fracture surface of pristine HN minicomposite specimen HNC3-1 (V_f = 16.8%, σ_c = 139 MPa, and $t_{rupture}$ = 404 hours), (e) side view of HNSC1-3 fracture surface, and (f) side view of precracked HNS minicomposite specimen HNSPC2-1 (V_f = 25.7%, σ_c = 247 MPa, and $t_{rupture}$ = 91 hours).

Failure in precracked minicomposites was caused by several mechanisms. First, the existence of cracks in the hot gage section had increased the local stress on the fibers that were bridging the cracks to a value of σ_c/V_f. The stress on the fibers was further increased because of the time-dependent fiber oxidation, which consumes SiC fibers to form silica (SiO_2). Second, other reactions had occurred including oxidation of the BN to form boria (B_2O_3) and oxidation of the SiC matrix to form SiO_2 within the cracks' surfaces. Boria liquid had reacted with silica and eventually formed solid-phase borosilicate glass that strongly bonded (embrittled) the fibers and matrix at the surfaces of the microcrack and bonded adjacent fibers together, causing embrittlement of the minicomposite. Figs. 15a and 15b show SEM images with energy dispersive X-ray spectroscopy (EDS) elemental composition (weight percent) of a point on the oxidation product within a crack on the side of precracked specimen HNSPC2-4 (V_f = 23.3%, σ_c = 201 MPa, 1200 °C) that had failed after 516 hours and a similar point on HNSPC1-2 (V_f = 34.5%, σ_c = 344 MPa, 1200 °C), which had failed after 8 hours, respectively. Borosilicate glass had filled the crack shown in Fig. 15a, where EDS analysis shows higher oxygen content in the vicinity of the CVI-SiC matrix crack. The formation of self-healing borosilicate glass here is due to the long stressed oxidation exposure time in air at 1200 °C. However, less oxide had formed in the crack in Fig. 15b, where EDS analysis shows lower oxygen content. This is due to the shorter exposure time of the CVI-SiC matrix crack to stressed oxidation in air at 1200 °C.

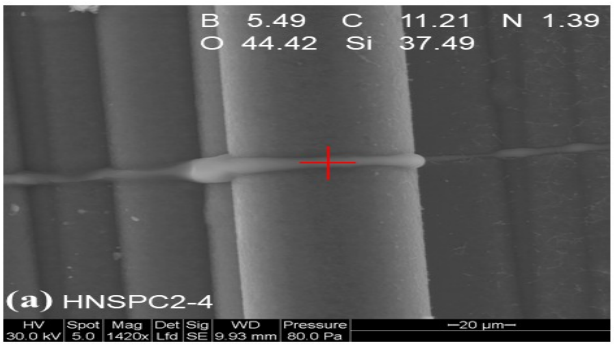

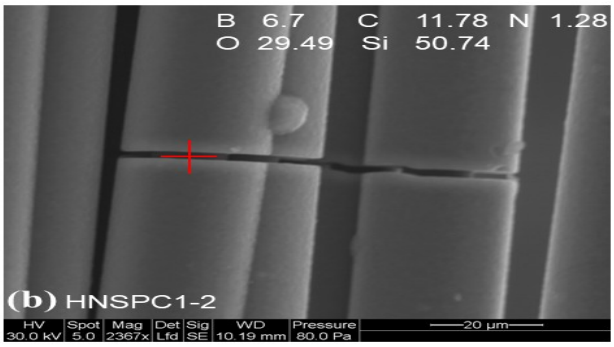

Fig. 15. SEM images with EDS elemental composition (weight percent) of a point on the oxidation product within a crack on the side of precracked HNS minicomposite specimens (a) HNSPC2-4 (V_f = 23.3%, σ_c = 201 MPa, and $t_{rupture}$ = 516 hours), and (b) HNSPC1-2 (V_f = 34.5%, σ_c = 344 MPa, and $t_{rupture}$ = 8 hours) that were tested in creep in air at 1200 °C.

Local fiber failure had occurred along the outermost oxidized crack surface once the fibers had reached a critical stress level. Failure of these fused (embrittled) fibers in the oxidized crack surface causes a planar (brittle) fracture surface as shown in Figs. 16 and 17 for HNS and HN minicomposites, respectively. Consequently, the stress increased on the remaining intact fibers in the interior, and ultimate failure occurred when those fibers could not withstand the additional load that was shed from the unbridged cracked region [23].

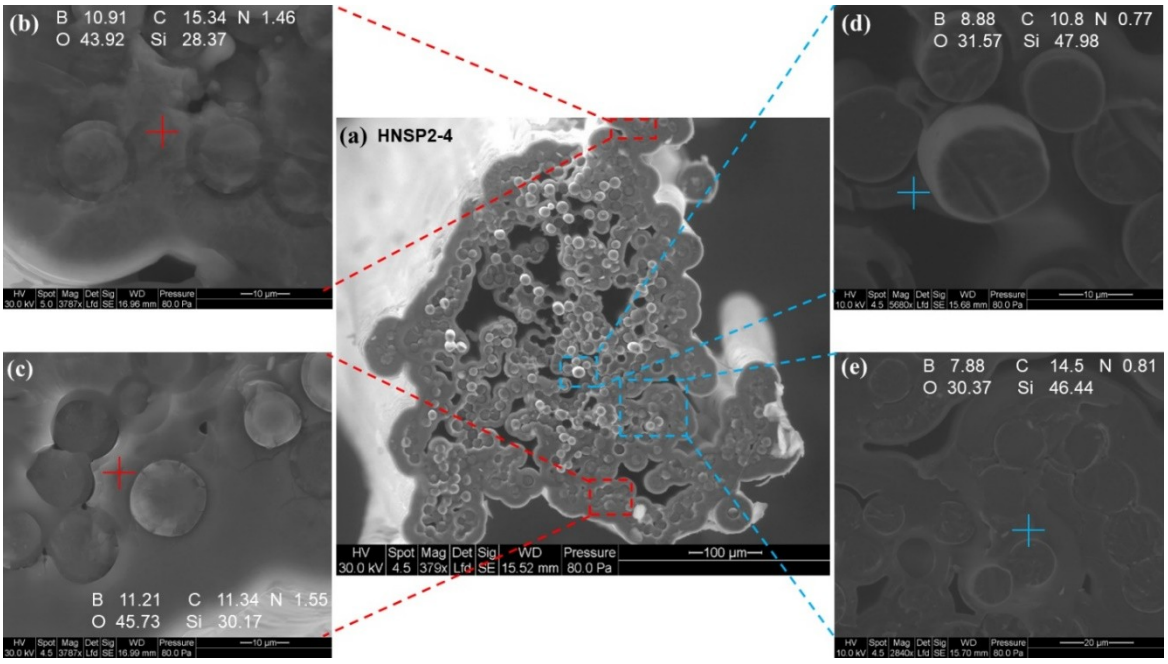

Fig. 16. (a) Low-magnification SEM image of fracture surface of precracked HNS minicomposite specimen HNSPC2-4 (V_f = 23.3%, σ_c = 201 MPa, and $t_{rupture}$ = 516 hours) that was tested in creep in air at 1200 °C. High-magnification SEM images with EDS elemental composition (weight percent) of selected points from near minicomposite surface in (b) and (c) and interior in (d) and (e) locations.

Formation of a self-healing borosilicate glass that fills matrix cracks is an interesting feature of the BN interphase. It reduced oxygen permeability and diffusion to the internal parts of the cracks and thus reduced the oxidation rate within the interior of the composite. Fig. 16 shows scanning electron micrographs with EDS elemental composition weight percent of various points on the fracture surface of precracked specimen HNSPC2-4 (V_f = 23.3%, σ_c = 201 MPa, 1200 °C) which had failed after 516 hours. Micrographs in Figs. 16b and 16c show

fracture surface oxidation with high oxygen content in the outermost fracture surface. The fracture surface is planar (Figs. 16b and 16c), with significant oxide formation between the fiber and matrix where most of the fibers appear to be fused to the matrix. The micrographs in Figs. 16d and 16e, however, show fracture surface oxidation with slightly lower oxygen content in the interior of the minicomposite. A planar fracture surface was still evident in Fig. 16d. However, the fibers had failed slightly above the planar surface in Fig. 16e. Similarly, the same behavior is observed in Fig. 17 in precracked specimen HNPC2-2 (V_f = 23.6%, σ_c = 149 MPa, 1200 °C), which failed after 65 hours. A planar fracture surface was again evident in the outer region in Fig. 17d. The oxygen content is higher in the outer region in Fig. 17d than in the inner region in Fig. 17b of the fracture surface. Furthermore, in both composite types, these observations indicate that the oxidation rate of the fracture surface is a function of crack depth, which agrees with previous work [22 and 23]. The small oxygen gradient observed between the outer and inner parts of the fracture surface demonstrates the BN interphase role in effectively limiting fiber and matrix oxidation and subsequent embrittlement in the interior part of those specimens. This was evidenced by the plane

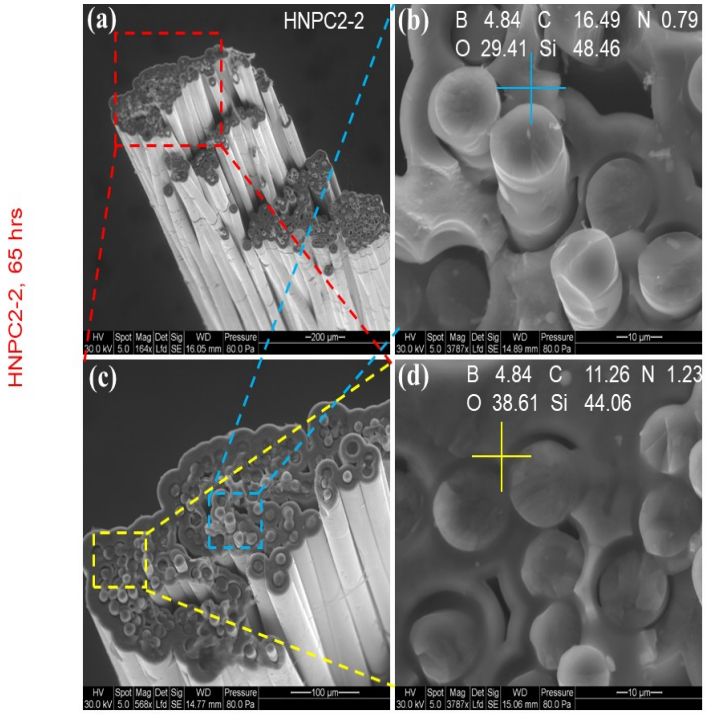

fibers' failure in (Figs. 16b, 16c, and 17d) and the fibers' failure at slightly above and slightly below the matrix fracture surface in Figs. 16d and 17b.

Fig. 17. Low-magnification SEM images in (a) and (c) of fracture surface of precracked HN minicomposite specimen HNPC2-2 (V_f = 23.6%, σ_c = 149 MPa, and $t_{rupture}$ = 65 hours), which was tested in creep in air at 1200 °C,

and high-magnification SEM images with EDS elemental composition (weight percent) of selected points from an (b) inner region and (d) outer region of the fracture surface.

5. Conclusions

The tensile creep behavior of pristine (uncracked) and precracked SiC_f/SiC ceramic matrix minicomposites containing different fiber types (HN and HNS) and fiber volume fractions (16%–43%) was investigated experimentally at 1200 °C in air, and the creep behavior of the uncracked minicomposites was modeled. When uncracked HN and HNS minicomposites were loaded below the matrix cracking stress at 1200 °C, damage accumulation (creep strain) was due solely to fiber and matrix creep, and ultimate failure was due to fiber or matrix creep rupture. More damage accumulation was observed in precracked HN and HNS minicomposites, resulting from enhanced creep of the fully loaded fibers and oxidation. The ultimate failure in precracked minicomposites occurred in the vicinity of the through-thickness crack due to oxidation that led to fiber embrittlement and creep rupture of the fully loaded fibers. HNS minicomposites were found to be more creep resistant than HN minicomposites, which is consistent with the effect of composition and microstructure on the resulting creep behavior of HN and HNS fibers. HN and HNS fibers have greater creep resistance than the matrix in the steady state creep regime. Consequently, HN and HNS fibers started carrying greater stresses than the matrix at 130 and 25 hours, respectively, in creep. Thus, the HN and HNS minicomposites' creep resistances increased with the increase in fiber volume fraction when minicomposites were loaded with the same global stress.

A new creep modeling approach was developed for both the primary and steady-state creep contributions of the fiber and matrix in uncracked uniaxial ceramic matrix composites. The model determines the change in load sharing for both constituents with time and resulting creep strain towards advancing the understanding of SiC_f/SiC composite's thermomechanical behavior and high temperature durability. The model was validated on two different fiber systems with considerable differences in creep behavior and a wide range of fiber volume fractions.

Fracture surfaces of uncracked HN and HNS minicomposites that failed during creep at 1200 °C in air while loaded below the matrix cracking stress showed clear fiber pullout; that is, little or no oxidation. In contrast, fracture surfaces of precracked HN and HNS minicomposites showed little to no fiber pullout and oxidation of the fibers, matrix, and interphase. As a result, a solid-phase borosilicate glass was formed during creep tests in the vicinity of CVI-SiC matrix through-thickness cracks, which had shortened the minicomposite life because of embrittlement.

Moreover, it was evident that there was a small oxidation gradient between the outer and inner regions of both HN- and HNS-reinforced precracked minicomposite fracture surfaces due to the crack healing behavior of BN interphase, which effectively limited fiber oxidation and embrittlement.

In order to maximize CMC durability in creep loading, the creep resistance of the fibers and the matrix need to be either equal or at least within the same order of magnitude. This will reduce the time-dependent stress redistribution and avoid overloading the constituent that is more creep resistant, thus extending the composite life in creep. In addition, the CMC must be operated at stresses that prevent matrix cracking, in order to prevent oxidation within a cracked region. The development and validation of life models for various types of CMCs under a variety of targeted specific application conditions (temperatures, loads, and environments) is an important area for additional research. Such models need to account for damage accumulation (strain) from the various mechanisms that occur during creep, fatigue, and oxidation and the resulting time-, temperature-, and environment-dependent varying stress state of each constituent. This would enable better understanding of the effect of the interaction between the different damage mechanisms and identify the most dominant mechanism that limits the life of such composites.

Acknowledgements

The authors gratefully acknowledge the National Aeronautics and Space Administration (NASA), USA for funding this work as a part of NASA's Transformational Tools and Technologies Project under NASA's Aeronautics Research Mission Directorate. Also, the authors would like to thank the Office of Naval Research USA for their additional funding of this work under ONR Grants N00014-11-10765 and N00014-14-1-0433. Additionally, the authors thank Mr. James D. Kiser from NASA Glenn Research Center for the insightful discussions and reviews. Moreover, the authors thank Mr. Ronald Phillips from HX5, LLC at NASA Glenn Research Center for his assistance in conducting creep tests of single fibers in vacuum. Finally, the authors thank Dr. Manigandan Kannan from the University of Akron for his expertise in scanning electron microscopy.

References

[1] A. Almansour, Characterizing ceramic-matrix composites to improve durability, Am. Ceram. Soc. Bull. 95 (2016) 35.

[2] J. Lamon, CVI SiC/SiC composites, in: N.P. Bansal (Ed.), Handbook of Ceramics Composites, Springer, Boston, MA, (2005), pp. 55–76.

[3] A. Almansour, E. Maillet, S. Ramasamy, G.N. Morscher, Effect of fiber content on single tow SiC minicomposite mechanical and damage properties using acoustic emission, J. Eur. Ceram. Soc. (2015) 3389–3399.

[4] A.W. Pryce, P.A. Smith, Matrix cracking in crossply ceramic matrix composites under static and fatigue loading, Acta Metall. Mater. 42 (1994) 861–870.

[5] A. Almansour, Use of single tow ceramic matrix minicomposites to determine fundamental room and elevated temperature properties, Electronic Thesis or Dissertation, University of Akron, OhioLINK Electronic Theses and Dissertations Center, (2017).

[6] J. DiCarlo, Creep limitations of current polycrystalline ceramic fibers, Technol. Compos. Sci. 51 (1994), 213–222.

[7] A.S. Nowick, B.S. Berry, Anelastic Relaxation in Crystalline Solids, Academic Press, New York, (1972).

[8] R. Raj, M.F. Ashby, On grain boundary sliding and diffusional creep, Met. Trans. 2 (1971) 1113–1127.

[9] H-M. Yun and J.A. DiCarlo, Comparison of the Tensile, Creep, and Rupture Strength Properties of Stoichiometric SiC Fibers, Cer. Eng. Sci. Proc., 20 [3], (1999), p. 259–272.

[10] J.A. DiCarlo, H.M. Yun, Non-oxide (Silicon Carbide) Fibers, in: Bansal N.P. (eds) Handbook of Ceramic Composites. Springer, Boston, MA, (2005), pp 33-52.

[11] S.M. Dong, G. Chollon, C. Labrugère, M. Lahaye, A. Guette, J. L. Bruneel, M. Couzi, R. Naslain and D. L. Jiang, Characterization of nearly stoichiometric SiC ceramic fibres, Journal of Materials Science 36 (2001) 2371–2381.

[12] C. Sauder, J. Lamon, Tensile creep behavior of SiC-based fibers with a low oxygen content, J. Am. Ceram. Soc. 90 (2007) 1146–1156.

[13] R. Bodet, X Bourrat, J. Lamon, and R. Naslain, Tensile creep behavior of a silicon carbide-based fiber with a low oxygen content, J Mater Sci. (1995);30:661–677.

[14] J. Lamon, Review: Creep of fibre-reinforced ceramic matrix composites, Int. Mater. Rev. (2019), pp. 1-35.

[15] H. M. Yun and J. A. DiCarlo, Time/temperature dependent tensile strength of SiC and Al2O3-based fibers, in Ceramic Transactions, Vol. 74, Advances in Ceramic-Matrix Composites III, edited by N. P. Bansal and J. P. Singh, American Ceramic Society (1996), pp. 17–26.

[16] G. N. Morscher, Tensile stress-rupture of SiCf/SiCm minicomposites with carbon and boron nitride interphases at elevated temperatures in air, J. Am. Ceram. Soc., (1997), 80, 2029–2042.

[17] J.A. DiCarlo, H.M. Yun, J.B. Hurst, Fracture mechanisms for SiC fibers and SiC/SiC composites under stress-rupture conditions at high temperatures, Appl. Math. Comput., 152 (2) (2004), pp. 473-481.

[18] A. Almansour, E. Maillet, G.N. Morscher, Tensile creep and rupture behavior of different fiber content and type single tow SiC/SiC minicomposites, in: D. Singh (Ed.), Mechanical Properties and Performance of Engineering Ceramics and Composites X: A Collection of Papers Presented at the 39th International Conference on Advanced Ceramics and Composites, John Wiley & Sons, Inc., Hoboken, NJ, 2015, pp. 11-19.

[19] B.B. Hill, C.E. Bakis, H.T. Hahn, Creep of SiC/ RBSN composite: analytical modeling, in: B.S. Newaz, G.M. Newaz, S. Mall (Eds.), Constitutive Behavior of High-Temperature Composites, ASME, New York, (1992), pp. 121–135.

[20] Y.H. Park, J.W. Holmes, Finite element modeling of creep deformation in fibre-reinforced ceramic composites, J. Mat. Sci. 27 (1992) 6341–6351.

[21] K.L. Rugg, R.E. Tressler, C.E. Bakis, J. Lamon, Creep of SiC/SiC microcomposites, J. Eur. Ceram. Soc. 19 (1999) 2285–2296.

[22] G. N. Morscher and J. D. Cawley, Intermediate temperature strength degradation in SiC/SiC composites, J. Eur. Ceram. Soc.,22(14–15), 2777–2788 (2002).

[23] G. N. Morscher, Stress-Environmental Effects on Fiber-Reinforced SiC-Based Composites, in: Ceramic Matrix Composites: Materials, Modeling and Technology (eds N. P. Bansal and J. Lamon), John Wiley & Sons, Inc., Hoboken, NJ, USA, (2014), pp 334-352.

[24] J. Martinez-Fernandez , G.N. Morscher, Room and elevated temperature tensile properties of single tow Hi-Nicalon, carbon interphase, CVI SiC matrix minicomposites, J. Eur. Ceram. Soc. 20 (2000) 2627–2636.

[25] V. H. Hammond, Creep Rupture of an Oxide/Oxide Composite Fiber, PhD Dissertation, University of Virginia, (2001).

[26] H. M. Yun, J. C. Goldsby and J. A. DiCarlo, Tensile creep and stress-rupture behavior of polymer derived SiC fibers, NASA TM-106692, (1994).

[27] C. Armani, Creep performance of oxide ceramic fiber materials at elevated temperature in air and in steam, PhD Dissertation, AFIT/DS/ENY/11-02, Graduate School of Engineering and Management, Air Force Institute of Technology (AU), Wright-Patterson AFB OH, March (2011).

[28] G.N. Morscher, Modal acoustic emission of damage accumulation in woven SiC/SiC at elevated temperatures, in: D.O. Thompson and D.E. Chimenti (Eds.), Review of Progress in Quantitative Nondestructive Evaluation, v18A, Kluwer Academic/Plenum Publishers, New York, (1999), pp. 419–426.

[29] J. Zhou, A.S. Almansour, G.G. Chase, G.N. Morscher, Enhanced oxidation resistance of SiC/SiC minicomposites via slurry infiltration of oxide layers, J. Eur. Ceram. Soc. 37 (2017) 3241–3253.

[30] J. Lamon, S. Mazerat, M. R'Mili, Reinforcement of ceramic matrix composites: Properties of SiC-based filaments and tows, in: N.P. Bansal and J. Lamon (Eds.), Ceramic Matrix Composites: Materials, Modeling and Technology, John Wiley & Sons, Inc., Hoboken, NJ, (2014), pp. 1-26.

[31] A.S. Almansour, SiC fibers and SiC/SiC ceramic matrix minicomposites damage behavior, in: Advanced Ceramic Matrix Composites: Science and Technology of Materials, Design, Applications, Performance and Integration, Engineering Conferences International, Inc., New York, (2017).

[32] H. M. Yun, J. C. Goldsby and J. A. Dicarlo, Effects of Thermal Treatment on Tensile Creep and Stress-Rupture Behavior of Hi-Nicalon SiC Fibers, NASA TM-107087, (1995).

[33] G.N. Morscher, Tensile creep and rupture of 2D-woven SiC/SiC composites for high temperature applications, J. Eur. Ceram. Soc. 30 (2010) 2209–2221.

[34] R. M. Sullivan, Time-dependent stress rupture strength of Hi-Nicalon fiber-reinforced silicon carbide composites at intermediate temperatures, J. Eur. Ceram. Soc. 36, (2016), 1885-1892.